PII: S0955-2219(98)00145-9

0955-2219/98/$—see front matter

Si_3N_4/SiCN Nanocomposites: Tensile Ductility and Rupture Behaviour

M. Mayne,[a] T. Rouxel,[b†] D. Bahloul-Hourlier[a] and J.-L. Besson[b*]

[a]LMCTS, ESA CNRS 6015, Université de Limoges, 123 Av. A. Thomas, 87060 Limoges, France
[b]LMCTS, ESA CNRS 6015, ENSCI, 47 Av. A. Thomas, 87065 Limoges, France

(Received 22 January 1998; accepted 16 June 1998)

Abstract

Tensile ductility and rupture behaviour of Si_3N_4/SiC composites were studied in the 1595 and 1640°C temperature range under strain rates of $5\times10^{-5}\,s^{-1}$ and $10^{-5}\,s^{-1}$. The behaviour was compared to that of Si_3N_4 monoliths containing the same initial α/β Si_3N_4 ratios with reference to an α-phase rich superplastic silicon nitride. The ductility of the composites was much smaller than that of the corresponding monoliths. It decreased when the SiC content increased and increased when the temperature was raised. Under a strain rate of $5\times10^{-5}\,s^{-1}$, ductility remained limited ($\varepsilon<25\%$) whatever the composition or the temperature, and failure occurred by slow crack growth. Contrary to the case of the α-phase rich superplastic silicon nitride for which the hardening was strain-enhanced and essentially time-independent, a dramatic change in hardening appeared and the ductility was markedly enhanced when the strain rate was lowered to $10^{-5}\,s^{-1}$. It was concluded that, under the higher strain rate, deformation was controlled by grain boundary sliding of the micro-sized Si_3N_4 grains. In this case, the SiC nanoparticles located along the grain boundaries hampered sliding of the Si_3N_4 grains, leading to a poor ductility. On the contrary, under the lower strain rate, the SiC nanoprecipitates contributed to the deformation and the ductility is improved.

*To whom correspondence should be addressed.

Now at Laboratoire Verres et Céramiques UMR CNRS 6512, Université de Rennes I, Campus Beaulieu, 35042 Rennes, France.

1 Introduction

Due to a unique combination of mechanical and chemical properties, silicon nitride based ceramics have received considerable attention as promising candidates for structural applications at elevated temperatures. However, trade-offs exist between these properties, and their optimisation with a view to a specific application remains a key challenge. For example, improved fracture toughness has been obtained either through the development of a self-reinforced microstructure or by the incorporation of a second phase. SiC is usually used in this case, in the form of particles, whiskers or fibres because of its high intrinsic properties and its chemical compatibility with Si_3N_4.

More recently, Si_3N_4/SiC nanocomposites[1] have been developed for which improvement of fracture toughness,[2–4] high temperature strength[5] and creep resistance[6,7] has been reported. But, superplastic behaviour has also been reported for such materials,[8,9] that is generally contradictory with a high creep resistance. It turns out that the effect of the incorporation of nanosized SiC crystals in a Si_3N_4 matrix is still not clearly understood and that further work is needed to clarify the influence of the nature of the starting materials, the size and distribution of the SiC nanoprecipitates on the development of the microstructure of the composites and the effect on mechanical properties.

Therefore, Si_3N_4/SiC micro/nano-composites have been processed to near full density using an amorphous SiCN precursor as a source of SiC nanoparticles. The influence of the processing parameters on the final microstructure has been detailed in a previous paper,[10] as was the compressive creep behaviour between 1200 and 1450°C.[11] In this paper, we focus on the tensile ductility and rupture behaviour of these materials

in a temperature domain (around 1600°C) where the corresponding monolith was proved to deform up to 80% elongation.[12]

2 Materials and Testing

2.1 Materials

The starting silicon nitride powder had a very high α-phase content (UBE SNE 10). It was mixed in ethanol with Y_2O_3 (Rhône–Poulenc, 99·995% pure) and Al_2O_3 (Lonza, 99·99% pure) as sintering aids. The composites were fabricated by adding nano-sized SiCN powder synthesized by laser pyrolysis of a mixture of SiH_4 and CH_3NH_2 gases[13] (atomic composition: Si = 48·1, C = 22·8, N = 26·2, O = 2·9; C/N atomic ratio = 0·87; specific area = 48 $m^2 g^{-1}$). The compositions of the green compacts are given in Table 1. The theoretical SiC contents in the composites were 10 and 20 wt%, respectively.[10]

The microstructure of the silicon nitride powder and of the SiCN nanoparticles have been described previously.[14,15]

The green compacts were hot-pressed for 2 h under 35 MPa using a BN coated graphite die operating in nitrogen. The hot-pressed billets were 40 mm in diameter and 5 mm thick. The sintering temperatures required to achieve nearly full density were 1600°C for the 10 wt% SiC composite and 1650°C for the 20 wt% SiC composite. The α/β ratio was estimated by X-ray diffraction analysis using the Cu $K_{\alpha 1}$ radiation by comparing the integrated intensity of the [201] peak for α-Si_3N_4 and the [200] peak for β-Si_3N_4.[16,17] The corresponding ratios were 30/70 and 0/100, respectively.

In order to try to separate the effect of the SiC nanoparticles from that of the matrix, Si_3N_4 monoliths were prepared by hot-pressing at 1600 and 1700°C to achieve α/β ratios of 30/70 and 0/100, respectively. Monoliths hot-pressed at 1550°C to retain the highest α/β ratio, for which the ductility had been studied previously,[12] were also fabricated to serve as a reference. The hot-pressing conditions are given in Table 1.

Microstructures were examined in a plane perpendicular to the pressing direction by scanning electron microscopy (SEM, JEOL JSM 35) after plasma-etching and by transmission electron microscopy (TEM, JEOL 2010). SEM micrographs of the different materials are shown in Fig. 1. The microstructure of Si_3N_4 monolith hot-pressed at 1550°C consisted of equiaxed grains of α-Si_3N_4 and slightly elongated grains of β-Si_3N_4 (in fact, β-$Si_{6-x}Al_xO_xN_{8-x}$ solid solution, but with a very low x due to the low alumina addition) embedded in an intergranular YSiAlON glass phase. The low sintering temperature limited grain growth and the mean grain size was ~250 to 300 nm. Yttrium was entirely concentrated in the intergranular amorphous phase that formed continuous intergranular films and pockets at triple grain junctions. When hot-pressing was carried out at 1700°C, the α to β-Si_3N_4 transformation was complete at the end of the treatment. The β-Si_3N_4 grains were acicular with a mean diameter of $0{\cdot}4 \pm 0{\cdot}1\ \mu$m and an aspect ratio ranging from 5 to 7.[18]

In the case of the 10 wt% SiC composite, the α-Si_3N_4 grains were equiaxed, but the β-Si_3N_4 grains were mostly equiaxed too, or at least presented a low aspect ratio, even if some of them had a more well-developed acicular morphology. The mean grain size was 360 nm. Most of the β-Si_3N_4 grains in the 20 wt% SiC composite were acicular but had an aspect ratio typically half that of the β-Si_3N_4 grains in the corresponding monolith. It seems that the SiC nanoprecipitates, though increasing the α to β-Si_3N_4 transformation rate, limit the acicular growth of the β-Si_3N_4 grains.[10] The SiC nanoparticles have sizes ranging from 30 to 60 nm. The precipitates were sometimes observed inside the Si_3N_4 grains. However, they were mainly located either along Si_3N_4 grain boundaries or, more often, they were gathered together into pockets (Fig. 2), the size of which was similar to that of the individual Si_3N_4 grains but could reach 1 to 1·5 μm. The SiC nanoparticles were well wetted by the amorphous phase so that a great fraction of the glass phase was localised in between the particles. As a consequence of this inhomogeneous distribution of the nanoparticles, numerous Si_3N_4–Si_3N_4 grain boundaries were free of SiC nanoparticles, and in this case, the intergranular glass films were very narrow ($\approx$ 1·3 nm). No other crystalline phases were detected either in the monoliths or the composites.

Table 1. Composition of the starting powder mixture, sintering temperature (Ts), theoretical SiC content and α/β Si_3N_4 ratio

Material	*Si_3N_4 (wt%)*	*Y_2O_3 (wt%)*	*Al_2O_3 (wt%)*	*SiCN (wt%)*	*Ts (°C)*	*Sic (wt%)*	*α/β Si_3N_4 ratio*
Monolith	91	6	3		1550	—	70/30
	91	6	3		1600	—	30/70
	91	6	3		1700	—	1/100
Composite	68·8	6	3	22·2	1600	10	70/30
	46·6	6	3	44·4	1650	20	0/100

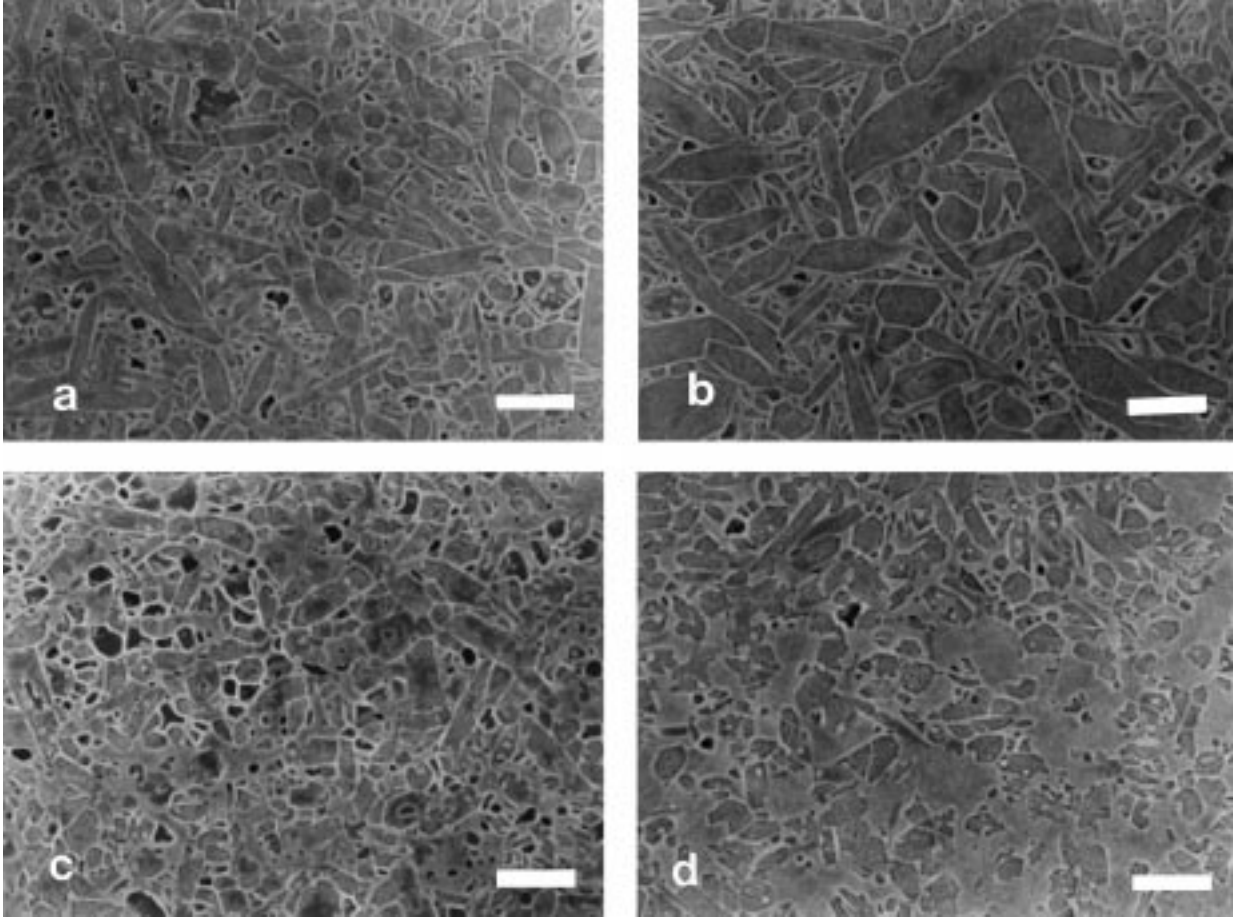

Fig. 1. Scanning electron micrographs of the materials after plasma etching (bar = 1 μm): (a) 30/70 monolith; (b) 0/100 monolith; (c) 10% SiC composite; (d) 20% SiC composite.

2.2 Testing

Dog-bone shape specimens with 10 mm long and 3 mm in diameter cylindrical gauges were used for tensile tests. The specimens were machined with diamond tools and the gauges polished finally with 0·3 μm diamond paste.

The experiments were conducted under nitrogen on an Instron 8562 testing machine equipped with a 1800°C furnace providing an isothermal zone 100 mm in length. The tests were carried out in a gas-tight chamber under nitrogen. SiC fixtures, pipes and pistons were used and diffusion bonding with the tensile grips was avoided by spraying BN powder on the specimen heads. The actual elongation during testing was recorded using a differential measurement device by means of a LVDT and mechanical contacts with the specimen. The heating and cooling rates were 10°C min^{-1}. The tensile tests were started after an isothermal hold of 45 min at the testing temperature to insure thermal stability.

Since large elongations were involved, true strain, ε_t, and true stress, σ_t, were calculated on the basis of a constant volume throughout the deformation:

$$\varepsilon_t = \ln(1 + \varepsilon) \tag{1}$$

$$\sigma_t = \sigma(1 + \varepsilon) \tag{2}$$

where ε is the nominal strain (or elongation), $\Delta l/l_0$, with l_0 initial gauge length and σ the nominal stress.

The experiments were conducted at constant strain rate by monitoring the crosshead speed, $\dot{\varepsilon}$, from the measurement of the elongation, ε:

$$\dot{\varepsilon}_t = \dot{\varepsilon}\frac{1}{1 + \varepsilon} \tag{3}$$

3 Experimental Results

3.1 Tensile curves

The deformed specimens had uniform elongation all along their gauge sections and the rupture always happened within the gauge. Their surfaces were smooth and free of cracks but were covered with a thin whitish layer which could be due to volatilisation of SiO gas from the YSiAlON liquid phase and/or to a slight active oxidation by oxygen atoms present in small quantity in the nitrogen gas. The resulting weight loss increased with the test duration and was at worst 0·6%.

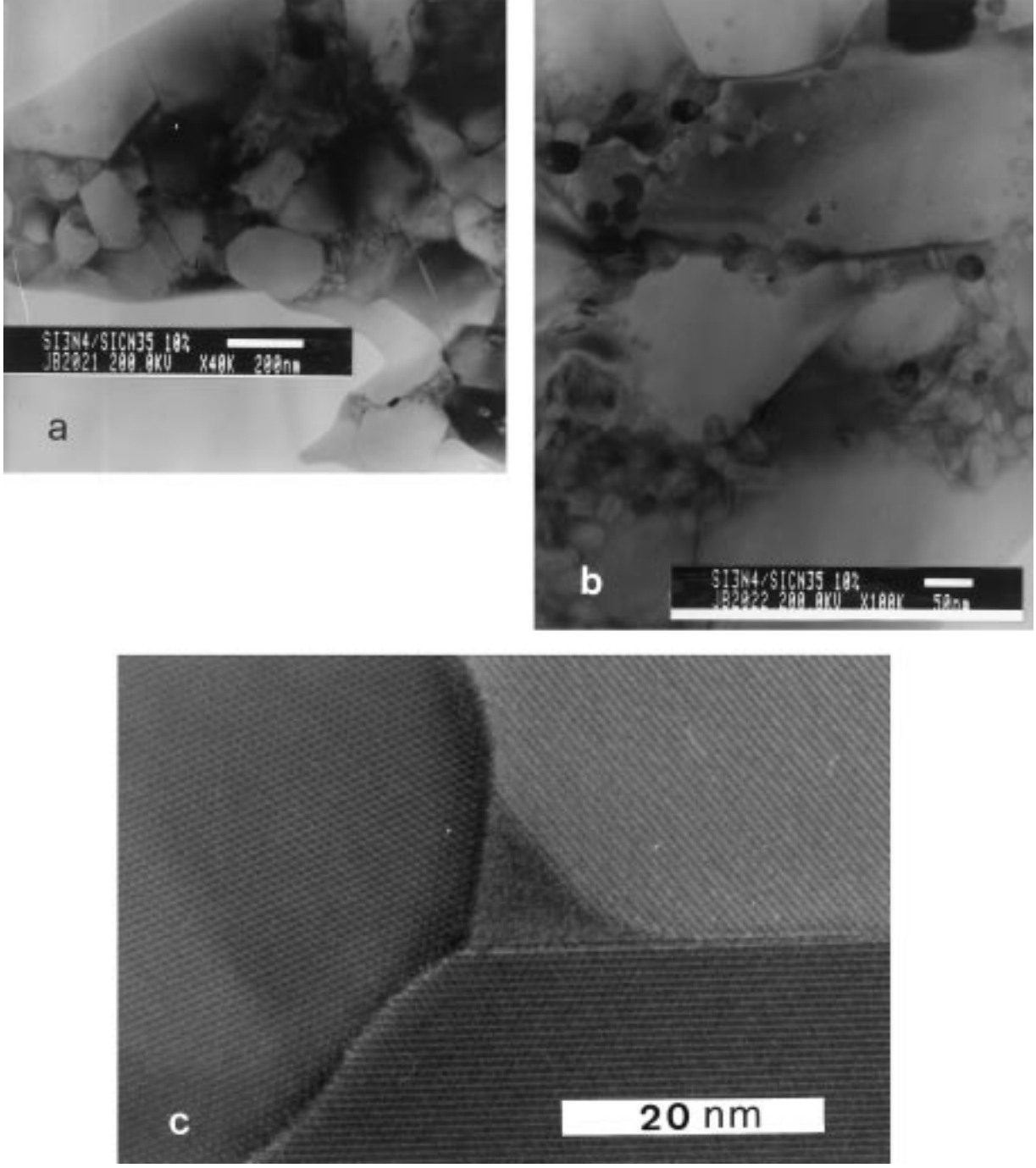

Fig. 2. Transmission electron micrographs of the 10% SiC composite: (a) general view (bar = 200 nm); (b) SiC nanoprecipitates along Si_3N_4 grain boundaries and in pockets (bar = 50 nm); (c) a glass pocket and grain boundaries free of SiC nanoprecipitates.

Tensile experiments were carried out at 1615°C with a constant strain rate of $5\times10^{-5}\,s^{-1}$ for the whole set of materials. Additional tests were made on the 10 wt% SiC composite at two other temperatures (1595 and 1640°C) with the same strain rate, and with a strain rate of $10^{-5}\,s^{-1}$ at 1615°C. The true stress – true strain curves are showed in Figs 3–5, respectively, and the experimental data are collected in Table 2.

3.1.1 Influence of composition

The tensile curves in Fig. 3 can be separated in two sets.

1. Those which show in the hardening stage an inflexion point that separates a regime of low hardening rate ($d\sigma/d\varepsilon$) from a regime of higher hardening rate: 70/30 and 30/70 monoliths. For these materials, the deformation at rupture is high ($\varepsilon > 60\%$) and a decrease in stress is observed before rupture occurs.
2. Those which are characterised by an unique hardening regime: 0/100 monolith, 10 and 20 wt% SiC composites. The deformation at rupture is lower than 25% and the rupture occurs at the maximum stress. A quasi-linear

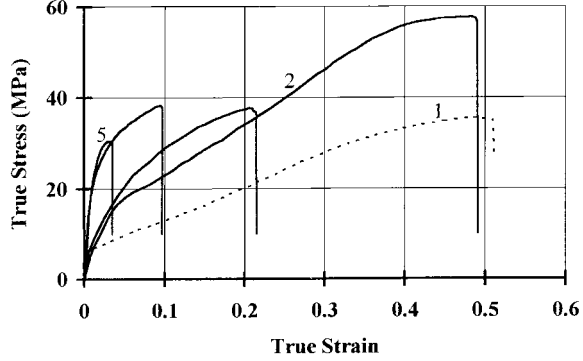

Fig. 3. Tensile true stress–true strain curves performed at 1615°C with a constant strain rate of $5\times10^{-5}\,s^{-1}$ on the different materials: (1) 70/30 monolith; (2) 30/70 monolith; (3) 0/100 monolith; (4) 10 wt% SiC composite; (5) 20 wt% SiC composite.

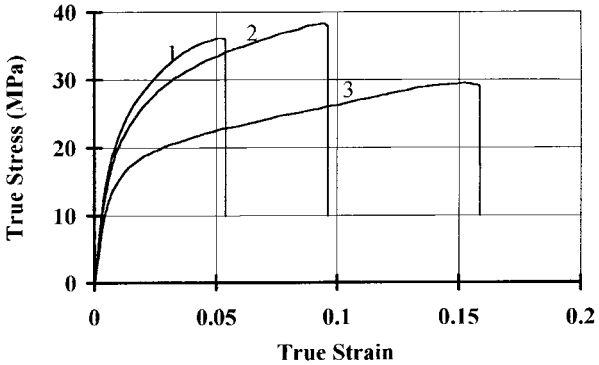

Fig. 4. Tensile true stress–true strain curves performed at different temperatures with a constant strain rate of $5\times10^{-5}\,s^{-1}$ on the 10 wt% SiC composite: (1) 1595°C; (2) 1615°C; (3) 1640°C.

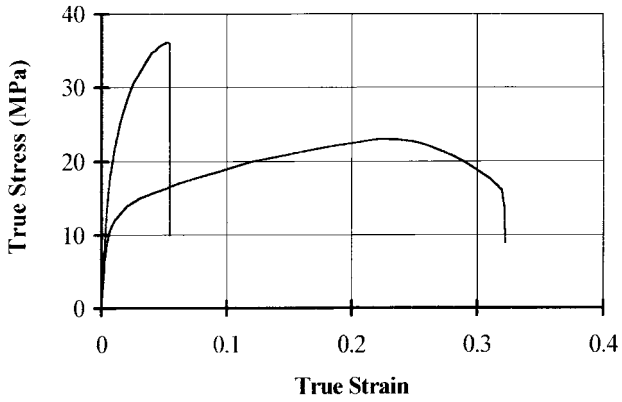

Fig. 5. Tensile true stress–true strain curves performed at 1615°C with different constant strain rates on the 10 wt% SiC composite: (1) $5\times10^{-5}\,s^{-1}$; (2) $10^{-5}\,s^{-1}$.

hardening rate ($d\sigma/d\varepsilon\sim130$ MPa) is reached for the 0/100 monolith and the 10 wt% SiC composite whereas the hardening rate decreases continuously in the case of the 20 wt% SiC composite.

3.1.2 Influence of temperature

The 10 wt% SiC composite was selected to investigate the influence of temperature under a strain rate of $5\times10^{-1}\,s^{-1}$ (Fig. 4). At 1595°C, the tensile curve is quite similar to the 20 wt% one tested at 1615°C. When the temperature is increased, the length of the pseudo-stationary hardening regime develops and the hardening rate decreases significantly from 130 to 80 MPa, reaching at 1640°C a value similar to that of the second regime of the 70/30 monolith tested at 1615°C. The elongation at rupture increases from 3·3% at 1595°C to 17·4% at 1640°C.

3.1.3 Influence of strain rate

When tested at 1595°C under a $10^{-5}\,s^{-1}$ strain rate, the 10 wt% SiC composite shows a tensile curve quite different from that obtained under $5\times10^{-5}\,s^{-1}$ (Fig. 5). The elongation at rupture is 7 times greater, the maximum stress 1/3 lower and the rupture happens after a significant decrease of the stress. Furthermore, the hardening rate in the pseudo-stationary hardening stage is low ($d\sigma/d\varepsilon\sim46$ MPa) and compares well with that of the first hardening regime of the 70/30 monolith (55 MPa at 1615°C under $5\times10^{-5}\,s^{-1}$).

3.2 Microstructural observations

3.2.1 Texture development and phase transformation

With regard to the testing temperatures, it is speculated that the α- to β-phase transformation goes on and that grain growth occurs with more and more acicular grains as the transformation proceeds. Moreover, in tension, the acicular grains must tend to align toward the tensile axis. Indeed, this trend had been observed in the case of the monoliths[12] though grain growth remained limited. The presence of a deformation texture was also corroborated by X-ray diffraction results which

Table 2. Experimental data from the tensile curves

Material	*Temperature (°C)*	$\dot{\varepsilon}_t\ (s^{-1})$	$\varepsilon_{rupture}\ (\%)$	ε_t	$\sigma_{max}\ (MPa)$	$d\sigma_t/d\varepsilon_t\ (MPa)$
70/30 monolith	1615	5×10^{-5}	66·5	0.510	35	55/83
30/70 monolith	1615	5×10^{-5}	61·2	0·480	55	110/123
0/100 monolith	1615	5×10^{-5}	24·6	0·220	37	130
10 wt% SiC composite	1615	5×10^{-5}	10·0	0·095	38	133
20 wt% Sic composite	1615	5×10^{-5}	3·3	0·033	30	—
10 wt% SiC composite	1595	5×10^{-5}	5·4	0·053	35	—
10 wt% SiC composite	1640	5×10^{-5}	17·4	0·160	29	80
10 wt% SiC composite	1595	10^{-5}	37·7	0·320	23	46

suggested that alignment of the c-axis toward the tensile axis occurred for the elongated β-Si_3N_4 grains but not for the equiaxed α-grains.

In the case of the 10 wt% SiC composite, tested under a strain rate of $5\times10^{-5}\,s^{-1}$, the changes in microstructure are even less pronounced than for the corresponding monolith. At the highest temperature used (1640°C) the number of elongated grains has increased but their aspect ratio remains low and their length is 1·2 to 1·5 μm [Fig. 6(a)]. This may be due either to the shorter durations of the tests or to the presence of the SiC nanoparticles. Differences between the deformed and undeformed microstructures become substantial in the case of the composite tested under a strain rate of $10^{-5}\,s^{-1}$ for which the majority of the grains are elongated and aligned toward the tensile axis [Fig. 6(b)]. In fact, even in this case where the duration of the test (7 h) is similar to that for the 70/30 monolith (9 h) the length of the acicular grains (1·2 to 1·9 μm) is significantly lower than that in the monolith (~2·5 μm). That suggests the SiC nanoparticles play a dominant role in the limitation of grain growth.

The development of a deformation texture makes difficult a quantitative analysis of the α/β ratio from massive samples. So, to get some insights into the effect of stress and temperature on the α- to β-phase transformation, the X-ray beam was always normal to a plan perpendicular to the hot-pressing direction and parallel to the applied stress, and the measurements were made on the gauge and on the heads of the specimens. The results are reported in Table 3. For the specimens tested under a strain rate of $5\times10^{-5}\,s^{-1}$, the data show a slow progress of the α- to β-phase transformation as the temperature increases, and the similarity of the results obtained from the gauges and the unstressed heads demonstrates the low effect of the applied stress on the transformation together with the absence of any significant texture. Hence, in the case of the composite tested at the lower strain rate, the difference in the α/β ratios between the gauge and the heads supports the development of a deformation texture as already suggested by the microstructural observations.

3.2.2 Rupture and damage

Typical fracture surfaces after failure are showed in Fig. 7. The materials can be separated in two groups.

1. Materials for which the fracture surface is divided in two parts: a smooth zone and a rough one. The 0/100 monolith and the composites tested under a strain rate of $5\times10^{-5}\,s^{-1}$ belong to this group. In these materials, the elongation at rupture is lower than 25% and failure occurs at the maximum stress.
2. Materials for which the fracture surface is very rough on the whole section. The 30/70 monolith and the 10 wt% SiC composite tested under a strain rate of $10^{-5}\,s^{-1}$ belong to this group. In these materials, the elongation at rupture is higher than 25% and failure occurs under a stress lower than the maximum stress.

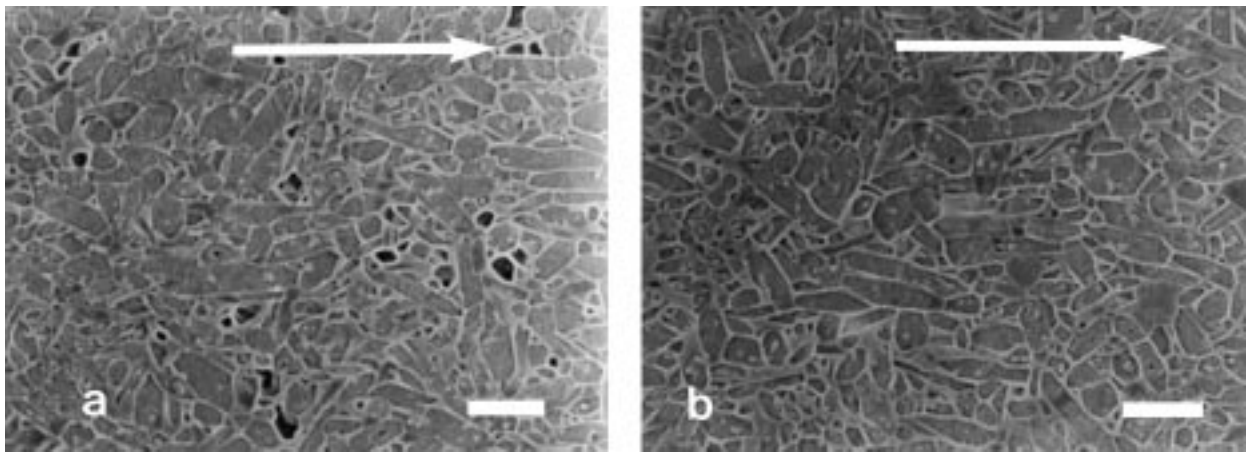

Fig. 6. Scanning electron micrographs of the 10 wt% SiC composite specimens (bar = 1 μm): (a) deformed at 1640°C under a strain rate of $5\times10^{-5}\,s^{-1}$ and (b) deformed at 1595°C under a strain rate of $10^{-5}\,s^{-1}$. The arrow indicates the direction of the tensile axis.

Table 3. α/β ratios in the deformed 10 wt% SiC composite specimens. The accuracy is estimated to be ~5%

Temperature	*1595°C*		*1615°C*		*1640°C*		*1595°C*	
Strain rate	$5\times10^{-5}\ s^{-1}$						$10^{-5}\ s^{-1}$	
α/β ratio	Head 25/75	Gauge 30/70	Head 15/85	Gauge 20/80	Head 13/87	Gauge 11/89	Head 10/90	Gauge 0/100

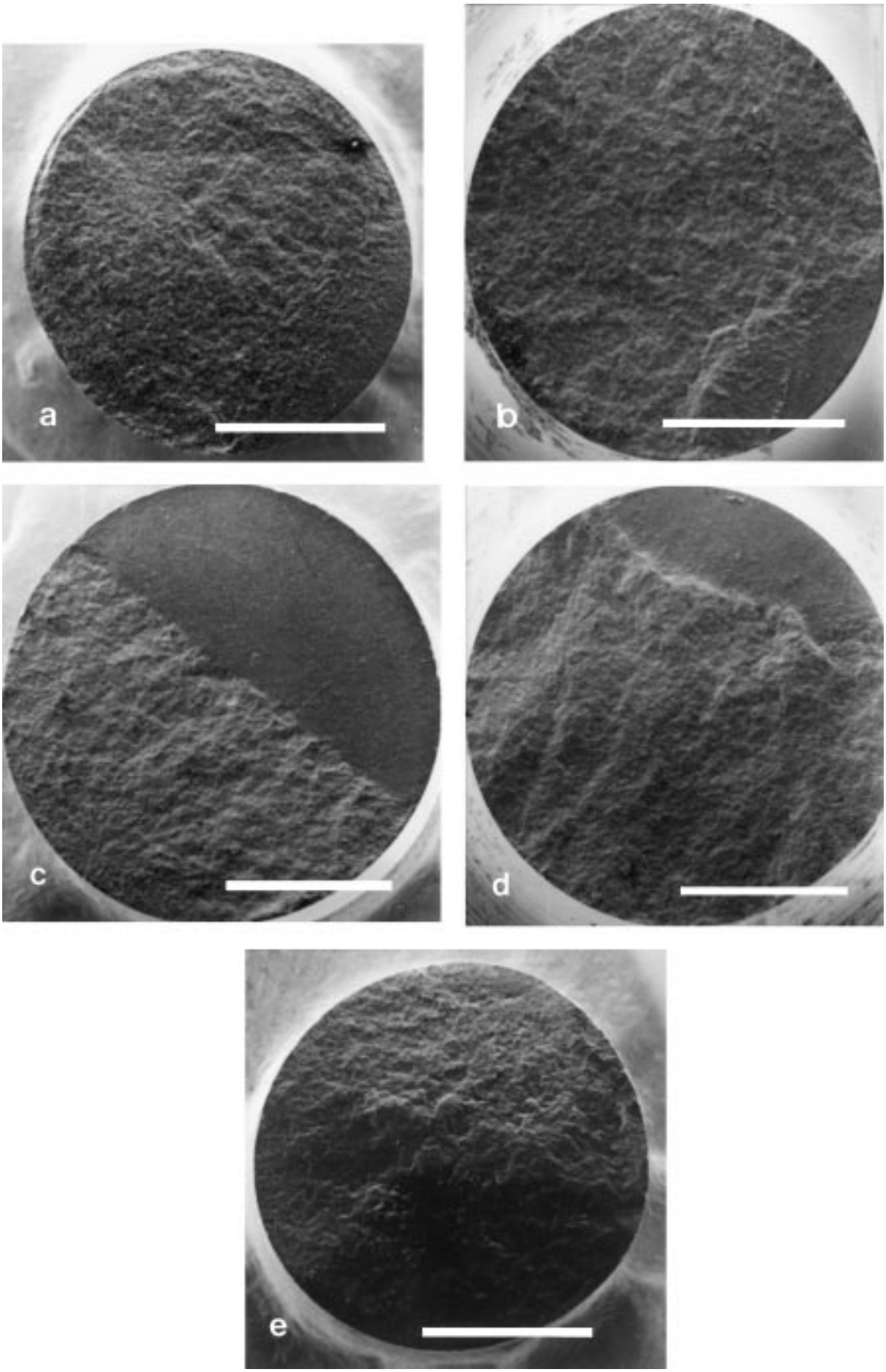

Fig. 7. SEM micrographs of fracture surfaces of tensile specimens (bar = 1 mm): deformed at 1615°C under a strain rate of $5\times10^{-5}\,s^{-1}$: (a) 30/70 monolith; (b) 0/100 monolith; (c) 10 wt% SiC composite; (d) 20 wt% SiC composite and (e) 10 wt% SiC composite deformed at 1595°C under a strain rate of $10^{-5}\,s^{-1}$.

Cavitation damage shows up on a polished section of the 10 wt% SiC composite tested under a strain rate of $10^{-5}\,s^{-1}$ (Fig. 8). A bimodal cavity size distribution is observed with small isolated spherical cavities ($<1\,\mu m$) and larger cavities ($\sim 3\,\mu m$) sometimes grouped together. Density measurements by helium pycnometry were made on the unstressed heads and on the gauge to evaluate the volume fraction of cavities in the composites. The change in density was only significant for the 10 wt% SiC composite tested under a strain rate of $10^{-5}\,s^{-1}$ and was found $\approx 1{\cdot}5\%$. To ascertain this result, Young's modulus measurements were performed using an ultrasonic technique.[19] According to Fate,[20] Young's modulus of silicon nitride is expressed by:

$$E = E_0\left(\frac{2\rho}{\rho_0} - 1\right) \tag{4}$$

where E and E_0 are Young's moduli of Si_3N_4 with density ρ and ρ_0, respectively.

Then, the volume fraction, p, of pores (or cavities) is given by:

$$p = \left(1 - \frac{E}{E_0}\right)/2 = 1 - \frac{\rho}{\rho_0} \tag{5}$$

The difference in Young's modulus between the heads and the gauge was found to be 3% for the 10 wt% SiC composite tested under a strain rate of $10^{-5}\,s^{-1}$, that leads to $p = 1{\cdot}5$, the same value as derived from density measurements.

These results are consistent with the results of the previous study on the monoliths[12] that showed that cavitation damage starts typically at 25 to 30% elongation and is accompanied by a decrease in the apparent applied stress as a result of a reduction of the effective cross-section area.

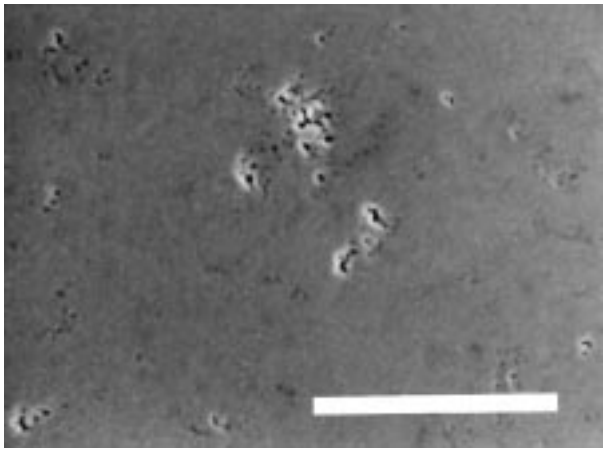

Fig. 8. Cavities in a polished gauge section of a 10 wt% SiC composite specimen tested at 1595°C under a strain rate of $10^{-5}\,s^{-1}$ (bar = 50 μm).

4 Discussion

The ductile deformation of the 70/30 monolith was discussed in our earlier work.[12,21] The conclusions are recalled here to serve as a starting point for the analysis of the behaviour of the materials concerned in the present study.

Four regions were identified on the tensile curve of 70/30 monolith. The first region corresponded to the elastic response. The second and the third regions were associated with regimes of permanent and uniform deformation and the fourth regime to a stage of cavitation damage. The hardening rate in region 2 was smaller than in region 3. It was concluded that deformation in region 2 was essentially controlled by the α-phase whereas it was controlled by the acicular β-grains in region 3. The transition between the two regions occurred for a volume fraction of α-phase of about 30%. The low hardening rate in region 2 was attributed to the equiaxed shape of the α-Si_3N_4 grains and to the transient liquid phase which accompanies the α- to β-phase transformation. In region 3, the strong hardening, with a quasi-linear hardening rate was related to the increase of the cross-linking degree in the acicular β-grain network and, to a lesser extent, to grain growth, that makes more difficult grain boundary sliding which is the major mechanism of superplasticity.[22]

These four regions can be identified in the tensile curve of the 30/70 monolith (Fig. 3) though region 2 is hardly marked due to an initial α volume content similar to that for which the transition between regions 2 and 3 happens.

For all the other materials, a single hardening region is observed, and, except for the composite tested under the lower strain rate, the damage region is not present. Under identical testing conditions, for the monoliths, the increase in hardening rate from 80 MPa (70/30) to 130 MPa (0/100) and the decrease in elongation at rupture from 66·5 to 24·6% can be associated with the increasing fraction of β-Si_3N_4 grains and to their increasing aspect ratio. The lower ductility of the 10 wt% SiC composite, compared to the 0/100 monolith, underscores the role of the SiC nanoparticles and of their distribution. Three arguments can be invoked to explain the role of the SiC particles. Firstly, a large amount of glass phase being trapped in the SiC grain pockets, the intergranular films are thinner than in the monolith. Secondly, sliding of the β-Si_3N_4 grains is hampered by the SiC particles located along the grain boundaries. Finally, the largest Si_3N_4 grains support the stress and the SiC particles gathered together in the pockets are essentially unstressed and do not participate to the deformation. This is accentuated by

an increase in the SiC content. On the contrary, an increase in the test temperature (Fig. 4), lowering the viscosity of the intergranular glass phase and possibly increasing its amount, facilitates grain boundary sliding, reduces the hardening rate and increases the deformation at rupture. In all cases, failure occurs at the maximum stress after a deformation of less than 25%, and the fracture surfaces show a well-demarcated rough region, associated to slow crack growth and a smooth region of a fast and essentially brittle fracture regime.

The behaviour of the 10 wt% SiC composite tested under a strain rate of $10^{-5}\,s^{-1}$ (Fig. 5) strongly differs from that of the other composites and in particular from that of the same material tested under a strain rate of $5\times10^{-5}\,s^{-1}$ at the same temperature (1595°C). The elongation at rupture is $\sim$ 38% instead of 5·4% and failure occurs after a cavitation stage as demonstrated by the changes in density and Young's modulus, the rough aspect of the entire fracture surface and the decrease in the stress during the ultimate stage of deformation. In addition, in this case, the α- to β-Si_3N_4 phase transformation is complete and the acicular β grains are aligned towards the tensile axis. Moreover, the hardening rate (46 MPa) is comparable to that observed in region 2 of the 70/30 monolith and contrasts with the hardening rate of the same material tested at $5\times10^{-5}\,s^{-1}$, that brings to the fore the role of the strain rate. When the strain rate is high, the Si_3N_4 grains interlock and the diffusion is too slow to release the stresses that appear at the buttressing points, that results in a poor ductility and a rupture essentially brittle. On the contrary, under a sufficiently low strain rate, enough time is provided to release the local stresses at the interlocking points and the acicular β-grains align towards the tensile axis. The stress is then transferred to the SiC nanoprecipitates and sliding becomes active between the rounded SiC particles inside the pockets. The fact that the hardening rate is comparable to that in region 2 of the 70/30 monolith, where deformation is controlled by sliding of equiaxed grains, supports this hypothesis.

In the light of the above developed arguments, a tentative explanation can be proposed for the stress peak observed by Kondo and co-workers[23] during the superplastic deformation of Si_3N_4 ceramic consisting of rod-shaped grains. In fact, the microstructure of their material consisted in rod-shaped β-Si_3N_4 grains (0·5 μm in average diameter and with an apparent aspect ratio of about 6) randomly orientated and in contact with each other, the space between the acicular β-Si_3N_4 grains being filled with smaller grains of about 200 nm. So, the microstructure of their material was very similar to that of our composites with the smaller grains playing in their case the role of the SiC nanoparticles in ours. Their tensile tests were conducted under a constant cross-head speed instead of a constant strain rate; therefore, the true strain rate decreased all along the test. Hence, we suspect the stress drop to be due to the transition from a deformation controlled by the rod-like β-grains to a deformation in which the contribution of the small nanosized grains becomes preponderant. It is noteworthy that the peak height is much smaller for the initial strain rate of $2\times10^{-5}\,s^{-1}$ and one may well wonder if any peak would have been observed in a test with an initial strain rate of $10^{-5}\,s^{-1}$. The higher flow stress in our samples may be linked to the incorporation of some carbon from the SiCN powder into the amorphous intergranular phase, enhancing its refractoriness.[11]

5 Conclusion

The tensile behaviour of Si_3N_4/SiC nanocomposites was investigated in a temperature range between 1595 and 1640°C under strain rates of $5\times10^{-5}\,s^{-1}$ and $10^{-5}\,s^{-1}$. The behaviour was compared to that of Si_3N_4 monoliths containing the same initial α/β Si_3N_4 ratios with reference to an α-phase rich superplastic silicon nitride.

The ductility of the composites was much smaller than that of the corresponding monoliths. It decreased when the SiC content increased and increased when the temperature was raised. Under a strain rate of $5\times10^{-5}\,s^{-1}$, ductility remained limited ($\varepsilon < 25\%$) whatever the composition or the temperature, and failure occurred by slow crack growth.

Contrary to the case of the α-phase rich superplastic silicon nitride for which the hardening was strain-enhanced and essentially time-independent, a dramatic change in hardening appeared when the strain rate was lowered to $10^{-5}\,s^{-1}$.

It was concluded that, under the higher strain rate, deformation was controlled by grain boundary sliding of the micro-sized Si_3N_4 grains whereas the SiC nanoprecipitates contributed to the deformation under the lower strain rate.

Acknowledgements

This work was supported by the CNRS in the frame of the GDR 1168 'Etude physico-chimique de poudres céramiques nanophasiques à base de silicium'. We are grateful to all the participants in the GDR for fruitful collaboration. We wish to thank Dr J.P. Erauw of VITO (Mol, Belgium) for the plasma etching of the SEM samples and

B. Soulestin (LMCTS) for his assistance in the preparation and observation of the TEM samples.

References

1. Niihara, K., New design concept of structural ceramics—ceramic nanocomposites. *J. Ceram. Soc. Jpn.*, 1991, **99**, 974–982.
2. Sawagushi, A., Toda, K. and Niihara, K., Mechanical and electrical properties of silicon nitride–silicon carbide nanocomposite material. *J. Am. Ceram. Soc.*, 1991, **74**, 1142–1144.
3. Sasaki, G., Nakase, H., Suganuma, K., Fujita, T. and Niihara, K., Mechanical properties and microstructure of Si_3N_4 matrix composite with nano-metre scale SiC particles. *J. Ceram. Soc. Jpn.*, 1992, **100**, 536–540.
4. Niihara, K., Hirano, T., Nakahira, A., and Izaki, K., The correlation between interface structure and mechanical properties for silicon nitride based nanocomposites. In *Grain Boundary Controlled Properties of Fine Ceramics*, eds. K. Ishizaki, K. Niihara, M. Isotani and R. G. Ford. Elsevier Applied Science, London, 1992, pp. 103–111
5. Niihara, K., Izaki, K. and Kawakami, T., Hot-pressed Si_3N_4–32% SiC nanocomposite from amorphous Si–C–N powder with improved strength above 1200°C. *J. Mater. Sci. Lett.*, 1990, **10**, 112–114.
6. Hirano, T., Niihara, K., Ohji, T. and Wakai, F., Improved creep resistance of Si_3N_4–SiC nanocomposites fabricated from amorphous Si–C–N precursor powder. *J. Mater. Sci. Lett.*, 1996, **15**, 505–507.
7. Rendtel, A., Hübner, H. and Herrmann, M., Creep behaviour of Si_3N_4/SiC-nanocomposite materials. In *Fourth Euro Ceramics. Basic Science—Trends in Emerging Materials and Applications*, Vol. 4, ed. A. Bellosi. Gruppo Editoriale Faenza Editrice S.p.A., Faenza, Italy, 1995, pp. 225–232.
8. Wakai, F., Kodama, Y., Sakaguchi, S., Murayama, N., Izaki, K. and Niihara, K., A superplastic covalent crystal composite. *Lett. to Nature*, 1990, **344**, 421–423.
9. Rouxel, T., Wakai, F. and Izaki, K., Tensile ductility of superplastic Al_2O_3–Y_2O_3–Si_3N_4/SiC composites. *J. Am. Ceram. Soc.*, 1992, **75**, 2363–2372.
10. Mayne, M., Bahloul-Hourlier, D. and Goursat, P., Si_3N_4/SiC(N) nanocomposites: influence of SiC(N) nanoprecipitates on the microstructure. In *Euro-Ceramics V*. Vols. 132–136, Part 2, cd. P. Abelard, A. Autissier, A. Bouquillon, J-M. Haussonne, A. Mocellin B. Raveau and F. Thevenot. Trans. Tech., Uetikon, Zürich, Switzerland, 1997, pp. 998–1001.
11. Besson, J.-L., Mayne, M., Bahloul-Hourlier, D. and Goursat, P., Nanocomposites Si_3N_4/SiCN: influence of SiC nanoprecipitates on the creep behaviour. In *Euro-Ceramics V*, Vols. 132–136, Part 3, ed. J. Baxter, L. Cot, R. Fordham, V. Gabis, Y. Hellot, M. Lefevbre, H. Le Doussal, A. Le Sech, R. Naslain and A. Sevagen. Trans. Tech., Switzerland, 1997, pp. 1970–1973.
12. Rouxel, T., Rossignol, F., Besson, J-L. and Goursat, P., Superplastic forming of an α-phase rich silicon nitride. *J. Mater. Res.*, 1997, **12**, 480–492.
13. Luce, M., Croix, O., Robert, C. and Cauchetier, M., Laser synthesis of ultrafine Si/C/N composite powders. In *Ceramic Powder Science III*, *Ceramic Transactions*, Vol. 12, ed. G. L. Messing, S. I. Hirano and H. Hausner, The American Ceramic Society, Westerville, OH, 1990, pp. 267–274.
14. Madigou, V., Monthioux, M. and Oberlin, A. Microstructure et microtexture d'un composite Si_3N_4 renforcé whiskers SiC et de ses constituents. In *Actes du Colloque, Matériaux composites pour applications à hautes températures*. ed. R. Naslain, J. Lamalle and J-L. Zulian. AMAC, Paris, 1990, pp. 221–235.
15. Monthioux, M. and Béraud, C., private communication; details can be found in Mayne, M., Elaboration, microstructure et comportement au fluage de nanocomposites Si_3N_4/SiC. Doctorate thesis, Université de Limoges, France, 1997.
16. Rossignol, F., Goursat, P., Besson, J-L. and Lespade, P., Microstructure and mechanical behaviour of self reinforced Si_3N_4 and Si_3N_4–SiC whisker composites. *J. Eur. Ceram. Soc.*, 1994, **13**, 299–312.
17. Gazzara, C. P. and Messier, D. R., Determination of phase content of Si_3N_4 by X-ray diffraction analysis. *Am. Ceram. Bull.*, 1977, **56**, 777–780.
18. Rossignol, F., Nitrure de silicium monolithique et composites à fibres courtes Si_3N_4/SiC_f: relations microstructure–renforcement–déformation plastique à haute température. Doctorate thesis, Université de Limoges, France, 1995.
19. Gault, C., Ultrasonic non destructive evaluation of microstructural changes and degradation of ceramics at high temperature. In *Nondestructive Monitoring of Materials Properties*, ed. J. Holbrook and J. Bussière. *Materials Research Society Symposium Proceedings*, Vol. 142, Pittsburg, PA, 1989, pp. 263–274.
20. Fate, W. A., High-temperature elastic moduli of polycrystalline silicon nitride. *J. Appl. Phys.*, 1975, **46**, 2375–2377.
21. Rossignol, F., Rouxel, T., Besson, J-L., Goursat, P. and Lespade, P., Superplasticity in silicon nitride through the α to β phase transformation. *J. Phys. III France*, 1995, **5**, 127–134.
22. Langdon, T. G., An evaluation of the strain contributed by grain boundary sliding in superplasticity. *Mater. Sc. Eng*, 1994, **A174**, 225–230.
23. Kondo, N., Wakai, F., Nishioka, T. and Yamakawa, A., Superplastic Si_3N_4 ceramics consisting of rod-shaped grains. *J. Mater. Sci. Lett.*, 1995, **14**, 1369–1371.